Type-II hybrid order topological phase in a two-dimensional ferromagnetic bilayer

Jun-Hao Li, Ning-Jing Yang,* Zhi-Gao Huang, and Jian-Min Zhang†
Fujian Provincial Key Laboratory of Quantum Manipulation and New Energy Materials, College of Physics and Energy, Fujian Normal University, Fuzhou 350117, China

(Received 29 April 2026; revised 15 October 2026; accepted 5 November 2026; published 25 November 2026)

Realizing the coexistence of diverse topological phases and manipulating their transitions has been a subject of intense research interest in the field of topological materials. In this work, we leverage the distinct modulation of the band structure induced by valley-layer coupling and sliding ferroelectricity in two-dimensional bilayer van der Waals materials and uncover stepwise topological phase transitions in a bilayer ferromagnetic MX_2 system, utilizing ScI_2 as an ideal platform. Notably, we propose utilizing the valley-layer coupling characteristics of the selected bilayer material that differ from antiferromagnetic ones; we reveal that this specific magnetic configuration hosts a rich variety of topological states, including a second-order topological insulator (SOTI), a Type-II hybrid-order topological insulator (Type-II HyOTI), and a high-Chern-number quantum anomalous Hall insulator (HC-QAHI) with $C = 2$ and a quantum anomalous Hall insulator (QAHI) with $C = 1$. By tuning the applied strain, we systematically control the phase transitions within the system and introduce a topological index to characterize this layer-projected topological framework. Additionally, we evaluate the anomalous Hall conductivity to distinguish the transport signatures of topological phases with different Chern numbers, thereby offering predictive insights for the experimental realization and modulation of topological quantum devices.

DOI: 10.1103/hrmc-wzkq

I. INTRODUCTION

Topological insulators and their associated phase transitions play a pivotal role in modern condensed matter physics and quantum computing [1–7]. Recently, magnetic topological materials [8–11] and higher-order topological insulators (HOTIs) [12–18] have emerged as a research frontier, with the discovery of a hybrid-order topological insulator (HyOTI), where lower-order and higher-order topological states coexist, marking a significant breakthrough [19–25]. While HyOTI was first observed in phononic crystals [20] and later in 3D electronic systems [21] like elemental arsenic [22], the realized hybrid order typically features the coexistence of first and higher-order topological states within the same energy spectrum, which cannot be trivially decoupled into two independent subspaces in the energy domain. This concept has recently been extended to 2D electronic materials [24,25]. The recent discovery of sliding ferroelectricity in two-dimensional van der Waals materials has introduced a versatile degree of freedom for manipulating electronic properties [26–30]. Unlike conventional ferroelectrics, the vertical polarization in these systems is coupled to the interlayer stacking order [31], allowing for nonvolatile switching via mechanical sliding, in which sliding ferroelectricity combined with mechanical strain and different correlation strengths has been shown to induce various topological phase transitions [24,32–35]. Nonetheless, there is still a lack of in-depth research on whether such materials have more abundant topological states under different magnetic configurations.

Motivated by these developments, exploring the rich physical properties of hybrid-order topological materials has become an innovative research direction in condensed matter physics. Prior research has identified the existence of a hybrid-order topological state within a single band gap, and a spin hybrid-order topological insulator (SHTI) characterized by a layer-spin locking mechanism, in bilayer antiferromagnetic (AFM) structures [24]. In this work, a HyOTI featuring hybrid orders within different band gaps is designated as a Type-I HyOTI. Notably, driven by the influence of sliding ferroelectricity, the system exhibits a rich variety of topological phases under applied strain. Consequently, recognizing the immense potential of sliding ferroelectricity in generating and manipulating diverse topological phases [36–38], we aim to investigate whether additional topological phases and rich physical phenomena can emerge in different structural configurations.

In this work, we extend the mechanism of sliding ferroelectricity-induced topological phase transitions to the bilayer ferromagnetic (FM) MX_2 system. Bilayer ferromagnetic structures were selected for this investigation because of the valley-layer coupling characteristics. Driven by the influence of sliding ferroelectricity and strain amplitude engineering, we can reveal the emergence of diverse topological states and phase transitions by employing strain engineering to drive band inversions. Furthermore, we have identified a HyOTI wherein the hybrid orders reside within the same band gap. We designate this state as a Type-II HyOTI to distinguish it from the aforementioned Type-I HyOTI. Meanwhile, we calculated the Berry curvature and its integral over the

*Contact author: ningjingyang99@gmail.com
†Contact author: jmzhang@fjnu.edu.cn

 ©2026 American Physical Society

Brillouin zone—the Chern number. We find that, owing to the unique properties of the FM structure, a special quantum anomalous Hall insulator (QAHI) phase with $C = 2$ can be obtained, and the Chern number exhibits a stepwise evolution across different topological phases. Consequently, by tuning between different topological phases within the same material, we can achieve distinct transport signatures, thereby offering a viable material strategy for realizing and manipulating novel topological phenomena. We also characterize the hybrid-order topological phase by analyzing the topological corner charge and combine it with the Chern number to distinguish other topological phases. We therefore introduce a topological invariant I_{FM} to represent different topological phases. As a result, we have achieved the coexistence of diverse topological phases within a single material platform, and provide a platform for exploring tunable topological phases and modulating their associated transport signatures.

II. COMPUTATIONAL METHODS

Density functional theory (DFT) calculations are performed using the Vienna *ab initio* simulation package (VASP) [39,40]. The exchange-correlation potential was described using the Perdew–Burke–Ernzerhof (PBE) generalized gradient approximation (GGA) functional [41]. The plane-wave cutoff energy is set to 500 eV. A centered 13 × 13 × 1 k-point mesh is used for structural relaxation, and a vacuum region larger than 15 Å is set to simulate two-dimensional (2D) materials. Atomic coordinates are fully relaxed until the force acting on each atom is smaller than 0.01 eV/Å, and the total energy converges to within 10^{-6} eV. The strong electron correlation effects for the localized d orbitals of Sc are treated by the DFT + U method [42,43] using U = 3. The vdW corrections are invoked through the DFT-D3 method [44]. Furthermore, a tight-binding Hamiltonian was derived from maximally localized Wannier functions (MLWFs), which were constructed using the Sc d orbitals as a basis via the WANNIER90 and WANNIERTOOLS codes [45,46]. More detailed results are available in the Supplemental Material [47] (see also Refs. [18,43,48,49]).

III. RESULTS AND DISCUSSION

In previous studies of MX_2 with AFM magnetic configurations [29,35,50–52], we found that the valley landscapes emerging under the influence of SOC and sliding ferroelectricity are diametrically opposite to those observed in the FM configuration, as shown in Fig. 1(a). Under the influence of spin–orbit coupling (SOC), both the AFM and FM structures exhibit valley polarization characterized by an SOC-induced potential difference (Δ_{SOC}). However, the different magnetic structures lead to distinct manifestations of this valley polarization. We can see that, because of the same direction of polarization of the magnetic moments in the upper and lower layers, the energy bands are degenerate in the absence of structural sliding in the left panel of Fig. 1(b). However, after the sliding operation, a ferroelectric potential difference (Δ_P) emerges at the same valley in the FM structure, as illustrated in the right panel of Fig. 1(b). Upon the sliding operation, the magnetic space group evolves from P-6′m′2 to P3m′1 for the AFM structure, and from P-6m′2′ to P3m′1 for the FM structure [53].

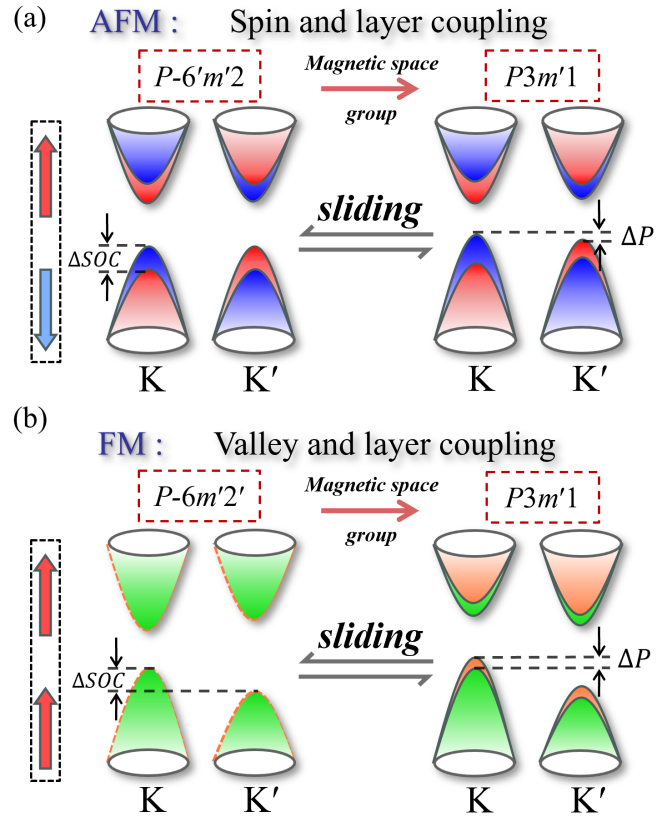


FIG. 1. Schematic (a) AFM spin-resolved and (b) FM layer-projected band structures at the K and K' valleys. Red and blue represent spin-up and spin-down, while orange and green denote the top and bottom layers, respectively.

We focus on the widely studied MX_2 materials with out-of-plane ferromagnetism. Notably, these materials belong to the D_{3h} point group symmetry. Their Hamiltonian can be written as a MoS_2-like three-band model, where the d-orbitals undergo crystal field splitting. Since the valence band maximum and conduction band minimum are primarily dominated by the d_{z^2} and $d_{xy}, d_{x^2-y^2}$ orbitals [54], we construct an effective model on the 2D honeycomb lattice incorporating only these specific orbitals. Employing the tight-binding approximation model, the Hamiltonian is expressed as follows:

$$\begin{aligned}\mathcal{H} = &\sum_{\langle ij\rangle}\sum_{\alpha\beta\tau} t_{ij}^{\alpha\beta}(1-\boldsymbol{\varepsilon})c_{i\alpha\tau}^{\dagger}c_{j\beta\tau} + \sum_{i\alpha\tau}\epsilon_{i\alpha}c_{i\alpha\tau}^{\dagger}c_{i\alpha\tau} \\ &+ \sum_{i\alpha\beta\tau}\boldsymbol{\lambda}_{\alpha\beta\tau}^{z}c_{i\alpha\tau}^{\dagger}c_{i\beta\tau} + \sum_{i\alpha\tau}\boldsymbol{P}_{\alpha}c_{i\alpha\tau}^{\dagger}c_{i\alpha\tau} \\ &+ \sum_{ij,\alpha\beta}\sum_{\tau\neq\tau'} t_{\perp}^{\alpha\beta}c_{i\alpha\tau}^{\dagger}c_{j\beta\tau'} + \mathrm{H.c.} \qquad (1)\end{aligned}$$

Here, $\alpha(\beta)$ represents different orbitals and $i(j)$ represents different sites, while $c_{i\alpha}(c_{j\beta}^{\dagger})$ denotes the electron annihilation (creation) operator and $t_{ij}^{\alpha\beta}$ denotes the nearest-neighbor-hopping amplitude between orbitals located at sites i and j. τ and τ' denote the layer indices, with $\tau \neq \tau'$ indicating two different layers in the bilayer system. $\boldsymbol{\varepsilon}$ denotes the magnitude

of the applied tensile strain. $\epsilon_{i\alpha}$ represents the onsite energy corresponding to each orbital. The atomic intrinsic SOC is described by $\boldsymbol{\lambda}^z_{\alpha\beta\tau} = \lambda L^z_{\alpha\beta} s^z_\tau$ on the third term. The next two terms describe the sliding induced ferroelectric potential and the interlayer coupling of the bilayer structure. Unlike the antiferromagnetic system, in which the spin operator is a 4×4 spin- and layer-projected matrix, the spin operator in the present system takes a different form. In the ferromagnetic bilayer, projection onto the same spin channel in both layers reduces the spin operator to a scalar factor multiplying the 2×2 identity matrix in layer space. Specifically, the effective model is constructed within a low-energy spin-polarized subspace, with the magnetization direction taken along the z axis. Starting from the spinful SOC Hamiltonian $H_{\mathrm{SOC}} = \lambda \boldsymbol{L} \cdot \boldsymbol{S} = \lambda(L_z S_z + L_x S_x + L_y S_y)$, we project it onto the retained spin state $|\uparrow_z\rangle$ using the projector $J_s = |\uparrow_z\rangle\langle\uparrow_z|$. Within this one-dimensional spin subspace, $J_s S_z J_s = \frac{1}{2} J_s$, while $J_s S_x J_s = J_s S_y J_s = 0$. Consequently, the projected SOC term becomes $H_{\mathrm{SOC}} = (\frac{\lambda}{2}) L_z$, with the spin degree of freedom reduced to a scalar factor rather than being replaced by the identity operator by assumption. Accordingly, the SOC matrix elements in Eq. (1) are $\boldsymbol{\lambda}^z_{\alpha\beta\tau} = (\lambda/2) L^z_{\alpha\beta}$, identical in both layers. For the sliding-induced ferroelectric term, $\boldsymbol{P}_\alpha = P_\alpha \sigma_z$, where σ_z is the Pauli matrix acting in layer space, giving opposite potential shifts in the two layers. The last term represents the interlayer coupling, $t_\perp$ is the hopping amplitude between different layers and its value is inversely proportional to the distance between atoms in different layers. Equation (1) in scalar form can account for the following matrix form:

$$H = H_0 + H_{\mathrm{SOC}} + H_P + H_\perp. \tag{2}$$

Here, H_0 represents the intralayer terms, corresponding to the first two terms of Eq. (1). H_{SOC} and H_p correspond to the third and fourth terms, accounting for the SOC and the sliding-induced ferroelectric potential. $H_\perp$ denotes the interlayer coupling term. For further details on the TB model, refer to the Supplemental Material [47].

We present a comparison of the evolution of tight-binding band structures under the influence of different terms. It is observed that the originally degenerate bands, which are plotted in Fig. 2(a), exhibit valley polarization at the K valley under the influence of SOC, as illustrated in Fig. 2(b). Furthermore, driven by the combined effects of the sliding ferroelectric potential and interlayer coupling, the layer-projected bands undergo layer splitting at the same valley, as shown in Fig. 2(c). This feature significantly facilitates subsequent band structure engineering.

Guided by the analysis of the theoretical model discussed above, we select the TMD MX_2 material family (M = Fe, Ru, Sc, Y; X = Cl, Br, I) as the target material for our subsequent investigation. The two-dimensional (2D) monolayer MX_2 with a hexagonal lattice belongs to the D_{3h} point group. Owing to the structural characteristics of TMD materials, spatial inversion symmetry ($\mathcal{P}$) is naturally broken; meanwhile, the ferromagnetism of the material investigated herein breaks time-reversal symmetry ($\mathcal{T}$). Upon breaking both symmetries, the system exhibits robust spin polarization and nontrivial topological properties. With the inclusion of spin–orbit coupling (SOC), the $SU(2)$ spin rotation symmetry

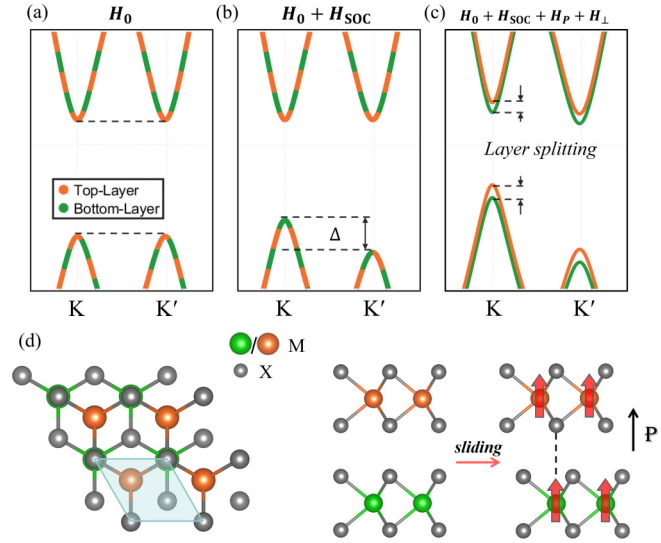


FIG. 2. Layer-projected band structures calculated using the ideal tight-binding model. The contributions from the top and bottom layers are represented in orange and green; (a) without SOC, ferroelectric potential, and interlayer coupling; (b) with SOC; (c) with SOC, ferroelectric potential, and interlayer coupling. Top and side views of the AB-stacked bilayer ScI_2 in (d) illustrate the interlayer sliding.

is broken, which, in conjunction with the broken time-reversal symmetry, gives rise to valley polarization. Furthermore, the sliding operation breaks the mirror symmetry (M_z), reducing the point group symmetry from D_{3h} to C_{3v}. This symmetry reduction serves as the direct physical origin of the sliding ferroelectricity in the material, and induces energy band splitting [55,56]. Building upon these properties, we construct a bilayer stacking configuration. However, the pristine bilayer MX_2 is protected by rotational and horizontal mirror (M_z) symmetries, which forbid spontaneous out-of-plane electric polarization. To overcome this, we introduce an interlayer sliding operation. Consistent with literature studies on the stacking orders of bilayer MX_2, we identify that the interlayer sliding operation $t_\parallel$ $[\frac{1}{3}, -\frac{1}{3}]$ from the AA-stacked configuration along the [110] direction leads to the AB-stacked phase [27,57]. Crucially, in the resulting AB-stacked configuration, the horizontal mirror symmetry (M_z) is broken, reducing the point group symmetry from the original D_{3h} to C_{3v}[29]. This symmetry reduction allows for the emergence of spontaneous out-of-plane electric polarization and energy band splitting, which is consistent with the results obtained from our previous tight-binding (TB) model analysis. In summary, based on the analyses of the electronic band structure and symmetry, we have demonstrated the possibility of achieving diverse topological phase transitions within the proposed material.

Through a comparative analysis of first-principles calculations, we observe that the band structure of bilayer ScI_2 at the K and K' valleys is remarkably clean and distinct. Furthermore, under the influence of the sliding ferroelectric mechanism, the potential energy differences at the valence band maximum (VBM) and conduction band minimum (CBM) of bilayer ScI_2 are $P_v = 30.35$ meV and $P_c = 18.44$ meV, respectively, and have values suitable for facilitating the subsequent engineering of band inversions and

topological phase transitions. Compared with other previously studied MX_2-family materials, such as $FeCl_2$ [35], $RuCl_2$ [50], and YI_2 [51], these characteristics make ScI_2 a more suitable candidate for realizing multiple topological phase transitions, and Yang *et al*. also reported on the topological phase transitions in AFM ScI_2 [24] (more details can be found in the Supplemental Material [47]). Therefore, we select the AB-stacked ferromagnetic bilayer ScI_2 as the target system in this work; the optimized lattice parameter is 3.95 Å and the interlayer distance is 3.655 Å.

We calculated the total energies for the ferromagnetic (FM), antiferromagnetic (AFM), and nonmagnetic (NM) states to determine the magnetic ground state. The system possesses the lowest energy in the ferromagnetic configuration, explicitly establishing it as the magnetic ground state. The computational results reveal that the $\Delta E_{\mathrm{MAE}} = E_{100}–E_{001}$ is –0.59 meV, indicating that the magnetic easy axis lies in-plane. However, given that the energy difference between the in-plane and out-of-plane directions is merely 0.59 meV, this exceedingly small magnetic anisotropy can be overcome experimentally. Out-of-plane magnetization may be stabilized by an applied out-of-plane magnetic field or exchange coupling to a magnetic substrate with perpendicular magnetic anisotropy. The reported topological phase diagram assumes an externally constrained out-of-plane magnetization, despite the calculated in-plane easy axis.

The top and side views of the AB-stacked structure and the schematics illustrating the structure before and after sliding are presented in Fig. 2(d). Subsequent calculations reveal an extremely low ferroelectric switching barrier (ΔE), which corresponds to the energy minimum along this sliding path, thereby confirming the AB configuration as the ground state. This suggests that driving ferroelectric domain switching via interlayer sliding under an external field is highly feasible under experimental conditions.

In summary, compared with other common members of the MX_2 family, we demonstrate that bilayer ferromagnetic ScI_2 with AB stacking serves as an ideal platform for realizing the desired topological phase transition. We select it as the optimal candidate for our further investigation.

Notably, the asynchronous feature of the transition gives rise to some intermediate phases where band inversion occurs in only one layer. We characterize this state by examining the coexistence of chiral edge currents and localized corner charges, and discuss its connection to hybrid-order topology in the context of broken mirror symmetry. Through systematic first-principles calculations, we aim to identify distinctive topological properties within the electronic band structures of the target material system. We employ strain engineering as the primary strategy to modulate the electronic band structure. Tensile strain is applied to the primitive lattice vectors a and b, denoted by the parameter $\boldsymbol{\varepsilon}$ in Eq. (1). We observe that as the strain amplitude increases, the valence band maximum (VBM) and conduction band minimum (CBM) of the top layer at the K valley undergo band inversion prior to those of the bottom layer. This results in an asynchronous band inversion. Upon further increasing $\boldsymbol{\varepsilon}$, an identical phenomenon is observed at the K' valley. We select five distinct topological phases for detailed analysis:

At $\boldsymbol{\varepsilon} = 1.75\%$ the system exhibits a second-order topological insulator (SOTI) phase. At this stage, band inversion has not yet occurred, and a gap opening in the edge states is observed, as illustrated in Figs. 3(a) and 3(f). Then, the system transitions to a hybrid-order topological insulator (Type-II HyOTI) phase. Here, the energy bands of the top Sc layer undergo inversion first, accompanied by the emergence of gapless edge states at $\boldsymbol{\varepsilon} = 2.23\%$, as illustrated in Figs. 3(b) and 3(g). At $\boldsymbol{\varepsilon} = 2.5\%$, band inversion occurs in both layers at the K valley. Consequently, the system evolves into a conventional first-order topological phase, specifically a quantum anomalous Hall insulator (QAHI). However, given that it possesses a high Chern number ($C = 2$) compared to conventional QAHIs, we designate this topological phase as a high-Chern-number QAHI (HC-QAHI), as illustrated in Figs. 3(c) and 3(h). Detailed discussions are provided in the following section. After that, asynchronous band inversion occurs in the top layer at the K' valley. This results in the coexistence of a first-order topological phase and a trivial phase at $\boldsymbol{\varepsilon} = 2.76\%$, but the system globally remains a QAHI, as shown in Figs. 3(d) and 3(i). Finally, at $\boldsymbol{\varepsilon} = 3\%$, band inversion occurs in both layers at the K' valley, rendering the entire system a trivial normal insulator (NI), as shown in Figs. 3(e) and 3(j).

After analyzing the energy spectra of the various topological phases, we find that the HyOTI realized in our system is distinct from those in previous studies [25]. Therefore, in this work, we define a HyOTI realized within the same band gap as a Type-II HyOTI, whereas those realized across different band gaps are defined as Type-I HyOTIs. Regarding hybrid order in different band gaps versus within the same band gap, different band gaps imply that the hybrid order is formed by higher-order and first-order topological states residing in distinct energy intervals, corresponding to Type-I HyOTI. Conversely, the same band gap indicates that the hybrid order is realized within a single energy interval, corresponding to Type-II HyOTI, meaning that both first-order edge states and higher-order corner states coexist within the exact same band gap in the energy spectrum.

To explicitly visualize the zero-energy corner or edge states—the hallmark of a 2D SOTI—we construct a real-space tight-binding model for a bilayer triangular nanoflake with the same Hamiltonian parameters, as shown in Fig. 4(a). In the SOTI phase, where both the top and bottom layers host second-order topological states, we observe that electrons are distinctly localized at the three corners of the triangular model. In the Type-II HyOTI phase, the electron localization pattern of the top layer is altered to exhibit edge states, whereas the bottom layer retains its localized corner states. Then, both the top and bottom layers exhibit edge states in the HC-QAHI phase. Subsequently, the top layer first transitions into a topologically trivial bulk state, while the bottom layer retains its original edge states. (The corresponding energy spectrum of the triangular flake is provided in the Supplemental Material [47].)

Having characterized the higher-order topological properties via fractional corner charges, we now employ the Chern number—the invariant of conventional topological insulators—to provide a more comprehensive description of the various topological phases. The Chern number is ob-

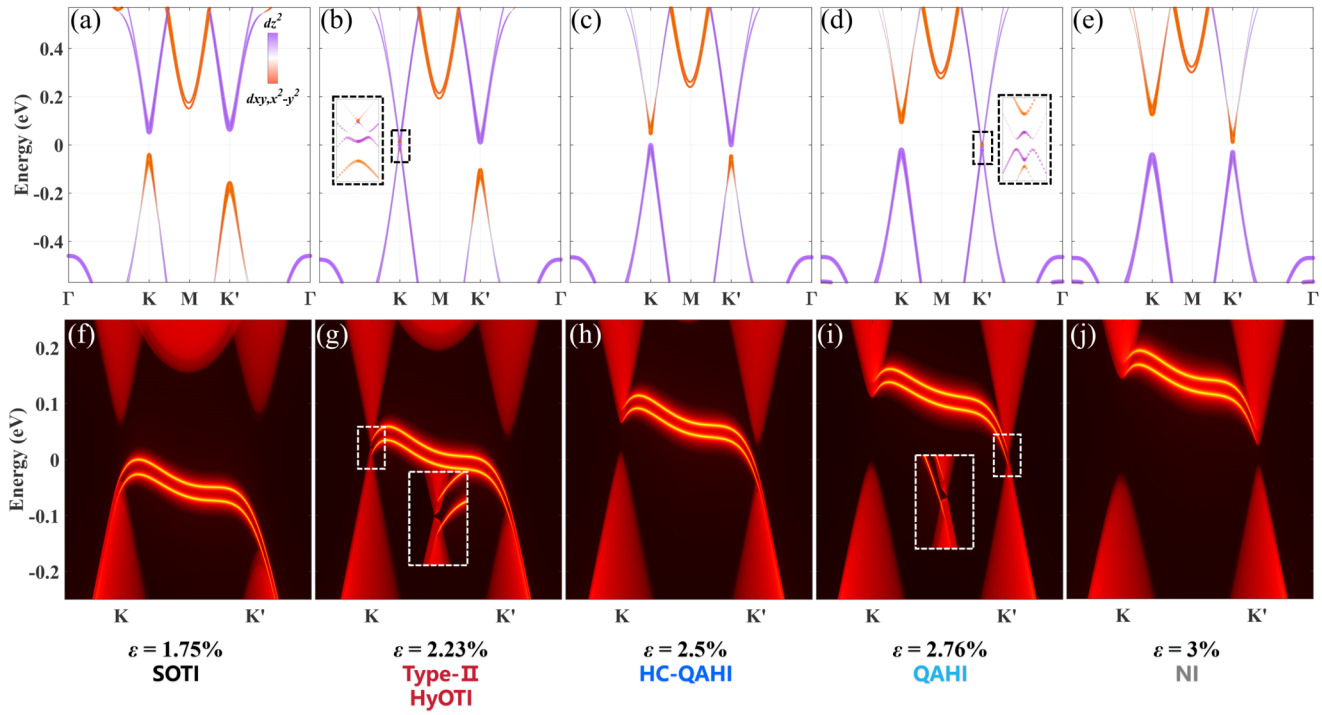


FIG. 3. (a)–(e) Orbital-resolved band structures of bilayer AB-stacked ScI_2 and (f)–(j) the surface states corresponding to the five topological phases under the modulation of tensile strain and sliding ferroelectricity.

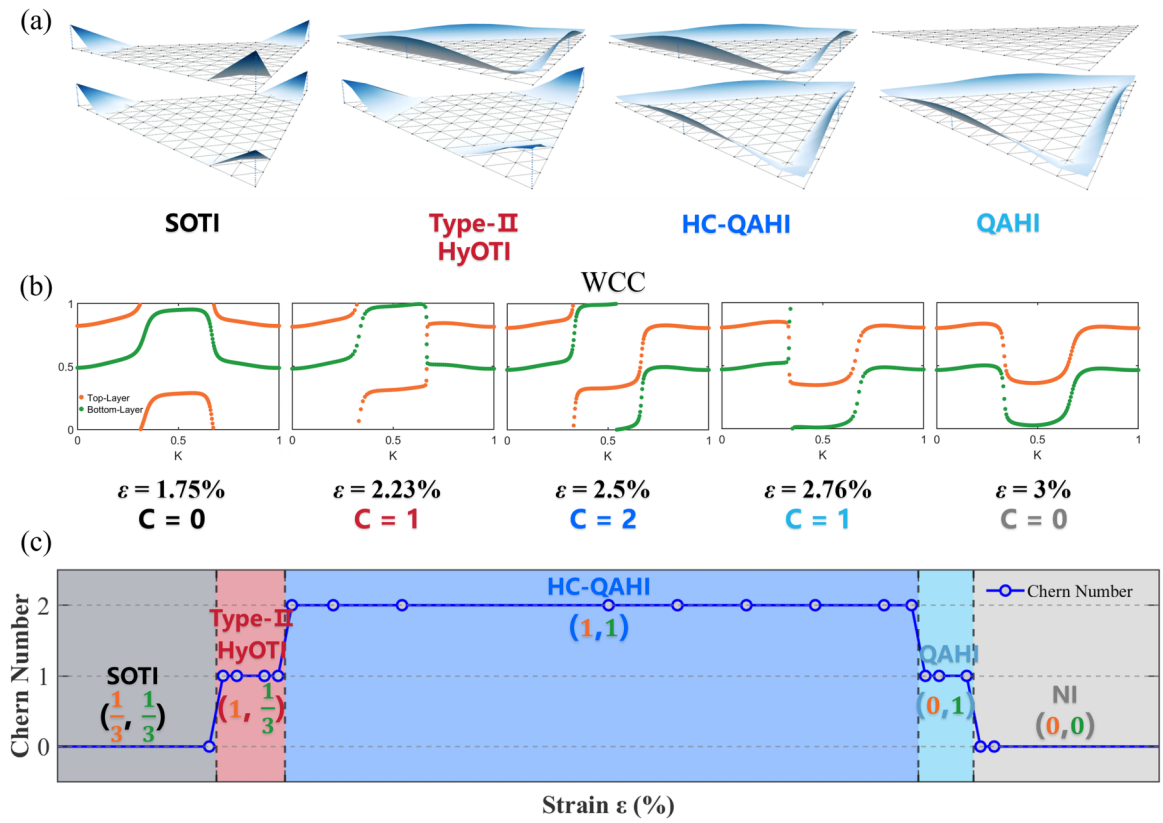


FIG. 4. (a) Evolution of real-space total charge distributions across distinct topological phases. The undulating blue waves represent the degree of electron localization in real space. (b) Under the modulation of tensile strain and sliding ferroelectricity, the evolution of layer-projected Wannier charge centers (WCCs). (c) Color-coded topological phase diagram and the corresponding Chern number evolution, showing the values of topological indices in different topological phases. Orange and green denote the topological indices $I_{\mathrm{FM}}^{\mathrm{top}}$ and $I_{\mathrm{FM}}^{\mathrm{bottom}}$ for the top and bottom layers, respectively.

tained by integrating the Berry curvature [$\Omega(\mathbf{k})$] over the first Brillouin zone (BZ) [58], $C_n = \frac{1}{2\pi}\int_{BZ}\Psi(\mathbf{k})dk_x dk_y$ The calculated C rigorously confirms its nature as a first-order topological insulator. Meanwhile, the WCCs are the eigenvalues derived from calculating the Wilson loop of the non-Abelian Berry connection, and their evolution with respect to k_y intuitively visualizes the nontrivial topology of the system. We calculated the evolution of the Wannier charge centers (WCCs) of the five signature topological phases in Fig. 4(b). We color-coded the contributions from different layers to clearly visualize the asynchronous evolution between layers, as shown in Fig. 4(c). In the SOTI phase, the WCCs of both the top and bottom layers return to their initial values along the wave vector path without crossing the unit cell boundary, corresponding to $C = 0$. In the Type-II HyOTI phase, the WCCs of the top layer cross the boundary and exhibit upward winding, while those of the bottom layer remain trivial, corresponding to $C = 1$. In the HC-QAHI phase, the WCCs of both layers simultaneously cross the boundary and wind upwards, corresponding to a total Chern number of $C = 2$. In the QAHI phase, the WCCs of the top layer revert to a topologically trivial state, while those of the bottom layer persist in winding, corresponding to $C = 1$. Finally, the WCCs of both layers return to the topologically trivial phase, corresponding to $C = 0$.

In this work, the top- and bottom-layer-projected band structures are shown in Fig. S2(c) within the Supplemental Material [47]. To characterize the layer-projected topology at finite interlayer coupling, we construct the projected layer operator $M(\mathbf{k}) = U^{\dagger}_{\mathrm{occ}}(\mathbf{k})\rho_z U_{\mathrm{occ}}(\mathbf{k})$, where U_{occ} contains the occupied Bloch states of the full bilayer Hamiltonian and $\rho_z = \mathrm{diag}(I_3, -I_3)$ distinguishes the two layers. The positive and negative eigenvalues of $M(\mathbf{k})$ define the top- and bottom-layer-projected sectors, respectively. These sectors are well defined provided that both the bulk energy gap and the spectral gap of $M(\mathbf{k})$ around zero remain open throughout the Brillouin zone. The corresponding topological indices are evaluated within these sectors, with the detailed definitions and interlayer-coupling analysis presented in the Supplemental Material [47]. Consequently, we use the layer-projected corner-charge index Q and Chern number C to characterize the topology of the corresponding projected sectors. Based on the analysis above, we establish a method to distinguish the five distinct topological phases. In this work, we define a layer topological index I_{FM} to classify these phases, constructed as the direct sum of the previously analyzed indices corner charge Q and Chern number C,

$$I_{\mathrm{FM}} = \left(I^{\mathrm{top}}_{\mathrm{FM}}, I^{\mathrm{bottom}}_{\mathrm{FM}}\right),$$
$$I^{\mathrm{top/bottom}}_{\mathrm{FM}} = Q^{\mathrm{top/bottom}} \oplus C^{\mathrm{top/bottom}} \tag{3}$$

where the top and bottom superscripts are employed to denote the layer-projected contributions to the topological indices. For noncentrosymmetric materials, the higher-order topological phase is protected by a C_n rotation symmetry [18]. The symmetry representations of the occupied energy bands, evaluated at the high-symmetry points (HSPs) of the first Brillouin zone (BZ), dictate this topological property. For C_3 rotation symmetry, we take $[K^{(3)}_n] = \#K^{(3)}_n - \#\Gamma^{(3)}_n$, where $\#K^{(3)}_n$ and $\#\Gamma^{(3)}_n$ represent the number of occupied bands with symmetry eigenvalue $e^{2\pi i(n-1)/3}$(for $n = 1, 2, 3$) at the K- and Γ-high-symmetry points, respectively [18,59]. The topological index of higher-order topological crystalline indicator and corner charge $Q^{(3)}_c$ are given by

$$\chi^{(3)} = \left([K^{(3)}_1], [K^{(3)}_2]\right),$$
$$Q^{(3)}_c = \frac{e}{3}[K^{(3)}_2] \ \mathrm{mod} e, \tag{4}$$

where e represents the charge of a free electron. Subsequently, we provide a comprehensive summary of the topological phase transitions, as illustrated in Fig. 4(a).

In general, the evolution of the five distinct topological phases is characterized by unique configurations of I_{FM}, $I^{\mathrm{SOTI}}_{\mathrm{FM}} = (\frac{1}{3}, \frac{1}{3})$, $I^{\mathrm{HyOTI}}_{\mathrm{FM}} = (1, \frac{1}{3})$, $I^{\mathrm{HC-QAHI}}_{\mathrm{FM}} = (1, 1)$, $I^{\mathrm{QAHI}}_{\mathrm{FM}} = (0, 1)$, $I^{\mathrm{NI}}_{\mathrm{FM}} = (0, 0)$. Here, the values $\frac{1}{3}$, 1, and 0 denote the higher-order topological state with $Q = \frac{1}{3}$, the first-order topological state with $C = 1$, and the trivial state, respectively. Most importantly, for the target system investigated here, the corner charge Q for either layer can only be $\frac{1}{3}$ or 0, while the Chern number C can only be 1 or 0; furthermore, neither the top nor the bottom layer can simultaneously host the first-order and higher-order topological states, which implies that Q and C cannot simultaneously take the values of $\frac{1}{3}$ and 1. To summarize the aforementioned step-like variations in the Chern number and the higher-order topological phase transitions discussed earlier, we constructed a comprehensive phase diagram. This diagram integrates the results from different characterization methods, utilizing distinct background colors and topological indices to denote the topological phases and step-like numerical values to represent the Chern number evolution, as shown in Fig. 4(c).

To show more details of the high-Chern-number QAHI and QAHI phases, we characterize the two QAHI phases further. This step is particularly crucial for distinguishing between the two QAHI phases at $\boldsymbol{\varepsilon} = 2.5\%$ and $\boldsymbol{\varepsilon} = 2.76\%$, which are difficult to distinguish effectively in the preceding analysis.

Using the Kubo formula, the Berry curvature can be written as [60,61]

$$\Omega(\mathbf{k}) = -\sum_{n}\sum_{n\neq m} 2f_n(\mathbf{k})\frac{\mathrm{Im}\langle\Psi_{n\mathbf{k}}|\hat{v}_x|\Psi_{m\mathbf{k}}\rangle\langle\Psi_{n\mathbf{k}}|\hat{v}_y|\Psi_{m\mathbf{k}}\rangle}{(E_{n\mathbf{k}} - E_{m\mathbf{k}})^2}, \tag{5}$$

here, $f_n(\mathbf{k})$ is the Fermi–Dirac distribution function, $\mathbf{k}$ is the electron wave vector, n and m are the band indices, and $\Psi_{n\mathbf{k}}$ is the Bloch wave function with eigenvalues E_n and E_m, respectively. $\hat{v}_x$ and $\hat{v}_y$ denote the velocity operators of the Dirac electrons. The velocity operators v_x and v_y in the Wannier basis are evaluated following the method of Yates *et al.* [62]. The calculated Berry curvature distributions for the two QAHI phases at $\boldsymbol{\varepsilon} = 2.5\%$ and $\boldsymbol{\varepsilon} = 2.76\%$ are presented in Fig. 5(b). The Berry curvature along high-symmetry paths is shown in Fig. 5(a). Evidently, at $\boldsymbol{\varepsilon} = 2.5\%$, the Berry curvature exhibits negative peaks at both the K and K' valleys. In contrast, at $\boldsymbol{\varepsilon} = 2.76\%$, the peak at the K valley vanishes, while the peak at the K' valley persists. As established, the nonzero Berry curvature functions as an effective magnetic field. However, these qualitative observations are insufficient to fully distinguish the two distinct topological phases; thus, a further quantitative characterization of the Berry curvature is required. The anomalous

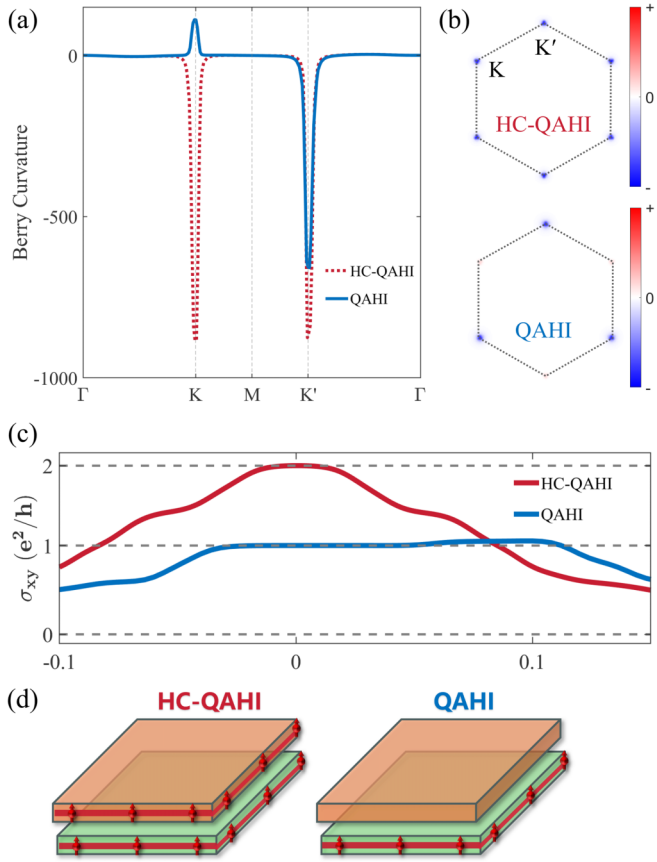


FIG. 5. (a) Berry curvature of bilayer AB-stacked ScI_2 along the high-symmetry lines and (b) Berry curvature of the HC-QAHI (top panel) and QAHI (lower panel) phases in the 2D k plane. (c) The AHC σ_{xy} of the HC-QAHI and QAHI phases in different colors. (d) Schematic plot of the topologically protected chiral edge states, HC-QAHI (left panel) and QAHI (right panel).

Hall current offers a potential pathway for information storage utilizing valley polarization, which can be verified through the anomalous Hall conductivity σ_{xy}.

For the target QAHI phase, σ_{xy} is quantized as an integer multiple of e^2/h, where the integer value is determined by the topological Chern number $\sigma_{xy} = C\frac{e^2}{h}$ and C denotes the topological Chern number, while e and h represent the elementary charge and the Planck constant, respectively. Consequently, the anomalous Hall conductivity σ_{xy}, corresponding to $\boldsymbol{\varepsilon} = 2.5\%$ and $\boldsymbol{\varepsilon} = 2.76\%$ are calculated, as illustrated in Figs. 5(b) and 5(c). The topologically protected dissipationless chiral edge states corresponding to $C = 2$ and $C = 1$ are illustrated in Fig. 5(d). It is evident that for the $C = 2$ phase, the chiral edge states in the top and bottom layers are propagating in the same direction. Thus, we establish an experimentally measurable scheme to effectively distinguish between the two topological phases at $\boldsymbol{\varepsilon} = 2.5\%$ and $\boldsymbol{\varepsilon} = 2.76\%$, both of which are characterized as QAHI phases. Crucially, we have realized the evolution of distinct Chern numbers within a single material system, offering possibilities for information storage in future quantum devices.

Existing investigations into hybrid orders have predominantly concentrated on antiferromagnetic systems, leaving the ferromagnetic regime largely unexplored. Crucially, from an experimental standpoint, two-dimensional ferromagnetic materials surpass their antiferromagnetic counterparts in terms of thermal stability, electrical transport performance, and the robustness of their electronic structures, and are significantly more accessible for experimental synthesis [63,64].

IV. CONCLUSIONS

In summary, inspired by the introduction of sliding ferroelectricity in two-dimensional antiferromagnetic systems, we reveal that the electronic band structure of ferromagnetic systems exhibits fundamental differences from those of their antiferromagnetic counterparts, transitioning from the conventional spin-layer coupling to valley-layer coupling, while some recent research has been devoted to the HyOTI. Under this framework, our comprehensive calculations demonstrate the emergence of five distinct topological phases within a single material platform, and we establish the tuning of these topological phase transitions via applied strain. Specifically, we have established bilayer ferromagnetic ScI_2 as a superior platform for manipulating topological states. By defining a unified topological index I_{FM}, we mapped a comprehensive phase diagram evolving from second-order topological insulators (SOTIs) to quantum anomalous Hall insulators (QAHIs), which include a Type-II HyOTI phase. Therefore, by introducing the valley-layer coupling mechanism into the study of the hybrid-order topological insulator, we believe our work not only broadens the landscape of exotic topological states but also provides critical theoretical predictions for future topological materials.

ACKNOWLEDGMENTS

This work is mainly supported by the National Natural Science Foundation of China (Grants No. 11874113, No. 62474041, and No. 12274078) and the Natural Science Foundation of Fujian Province of China (Grants No. 2025J02018 and No. 2023J01519).

DATA AVAILABILITY

The data that support the findings of this article are not publicly available. The data are available from the authors upon reasonable request.

[1] M. Z. Hasan and C. L. Kane, *Colloquium*: Topological insulators, Rev. Mod. Phys. **82**, 3045 (2010).
[2] X.-L. Qi and S.-C. Zhang, Topological insulators and superconductors, Rev. Mod. Phys. **83**, 1057 (2011).
[3] M. Z. Hasan and J. E. Moore, Three-dimensional topological insulators, Annu. Rev. Condens. Matter Phys. **2**, 55 (2011).
[4] M. Fruchart and D. Carpentier, An introduction to topological insulators, C. R. Phys. **14**, 779 (2013).

[5] A. Bansil, H. Lin, and T. Das, *Colloquium*: Topological band theory, Rev. Mod. Phys. **88**, 021004 (2016).

[6] F. D. M. Haldane, Nobel lecture: Topological quantum matter, Rev. Mod. Phys. **89**, 040502 (2017).

[7] J. E. Moore, The birth of topological insulators, Nature (London) **464**, 194 (2010).

[8] D. Xiao, W. Yao, and Q. Niu, Valley-contrasting physics in graphene: Magnetic moment and topological transport, Phys. Rev. Lett. **99**, 236809 (2007).

[9] Y. Tokura, K. Yasuda, and A. Tsukazaki, Magnetic topological insulators, Nat. Rev. Phys. **1**, 126 (2019).

[10] J.-M. Zhang, W. Zhu, Y. Zhang, D. Xiao, and Y. Yao, Tailoring magnetic doping in the topological insulator Bi_2Se_3, Phys. Rev. Lett. **109**, 266405 (2012).

[11] Y. Deng, Y. Yu, M. Z. Shi, Z. Guo, Z. Xu, J. Wang, X. H. Chen, and Y. Zhang, Quantum anomalous Hall effect in intrinsic magnetic topological insulator $MnBi_2Te_4$, Science **367**, 895 (2020).

[12] W. A. Benalcazar, B. A. Bernevig, and T. L. Hughes, Quantized electric multipole insulators, Science **357**, 61 (2017).

[13] W. A. Benalcazar, B. A. Bernevig, and T. L. Hughes, Electric multipole moments, topological multipole moment pumping, and chiral hinge states in crystalline insulators, Phys. Rev. B **96**, 245115 (2017).

[14] F. Schindler, A. M. Cook, M. G. Vergniory, Z. Wang, S. S. P. Parkin, B. A. Bernevig, and T. Neupert, Higher-order topological insulators, Sci. Adv. **4**, eaat0346 (2018).

[15] B. Xie, H.-X. Wang, X. Zhang, P. Zhan, J.-H. Jiang, M. Lu, and Y. Chen, Higher-order band topology, Nat. Rev. Phys. **3**, 520 (2021).

[16] F. Schindler, Z. Wang, M. G. Vergniory, A. M. Cook, A. Murani, S. Sengupta, A. Y. Kasumov, R. Deblock, S. Jeon, I. Drozdov, *et al.*, Higher-order topology in bismuth, Nat. Phys. **14**, 918 (2018).

[17] X.-L. Sheng, C. Chen, H. Liu, Z. Chen, Z.-M. Yu, Y. X. Zhao, and S. A. Yang, Two-dimensional second-order topological insulator in graphdiyne, Phys. Rev. Lett. **123**, 256402 (2019).

[18] W. A. Benalcazar, T. Li, and T. L. Hughes, Quantization of fractional corner charge in C_n-symmetric higher-order topological crystalline insulators, Phys. Rev. B **99**, 245151 (2019).

[19] X. Zhang, Z.-K. Lin, H.-X. Wang, Z. Xiong, Y. Tian, M.-H. Lu, Y.-F. Chen, and J.-H. Jiang, Symmetry-protected hierarchy of anomalous multipole topological band gaps in nonsymmorphic metacrystals, Nat. Commun. **11**, 65 (2020).

[20] Y. Yang, J. Lu, M. Yan, X. Huang, W. Deng, and Z. Liu, Hybrid-order topological insulators in a phononic crystal, Phys. Rev. Lett. **126**, 156801 (2021).

[21] Y.-Q. Zhu, Z. Zheng, G. Palumbo, and Z. D. Wang, Topological insulators with hybrid-order boundary states, Phys. Rev. B **111**, 195107 (2025).

[22] M. S. Hossain, F. Schindler, R. Islam, Z. Muhammad, Y.-X. Jiang, Z.-J. Cheng, Q. Zhang, T. Hou, H. Chen, M. Litskevich, *et al.*, A hybrid topological quantum state in an elemental solid, Nature (London) **628**, 527 (2024).

[23] S.-J. Huang, K. Park, and Y.-T. Hsu, Hybrid-order topological superconductivity in a topological metal $1T'$-$MoTe_2$, npj Quantum Mater. **9**, 21 (2024).

[24] N.-J. Yang, J.-M. Zhang, X.-P. Li, Z. Zhang, Z.-M. Yu, Z. Huang, and Y. Yao, Sliding ferroelectrics induced hybrid-order topological phase transitions, Phys. Rev. Lett. **134**, 256602 (2025).

[25] N.-J. Yang, Z. Huang, and J.-M. Zhang, Hybrid-order topological phase and transition in 1 *H* transition metal compounds, Appl. Phys. Lett. **125**, 263102 (2024).

[26] Z. Fei, W. Zhao, T. A. Palomaki, B. Sun, M. K. Miller, Z. Zhao, J. Yan, X. Xu, and D. H. Cobden, Ferroelectric switching of a two-dimensional metal, Nature (London) **560**, 336 (2018).

[27] M. Vizner Stern, Y. Waschitz, W. Cao, I. Nevo, K. Watanabe, T. Taniguchi, E. Sela, M. Urbakh, O. Hod, and M. Ben Shalom, Interfacial ferroelectricity by van der Waals sliding, Science **372**, 1462 (2021).

[28] P. Tang and G. E. W. Bauer, Sliding phase transition in ferroelectric van der Waals bilayers, Phys. Rev. Lett. **130**, 176801 (2023).

[29] Y. Feng, Y. Dai, B. Huang, and Y. Ma, Sliding ferroelectricity engineered coupling between spin Hall effect and layertronics in 2D lattice, J. Phys. Chem. Lett. **15**, 6699 (2024).

[30] M. Wu and J. Li, Sliding ferroelectricity in 2D van der Waals materials: Related physics and future opportunities, Proc. Natl. Acad. Sci. USA **118**, e2115703118 (2021).

[31] K. Yasuda, X. Wang, K. Watanabe, T. Taniguchi, and P. Jarillo-Herrero, Stacking-engineered ferroelectricity in bilayer boron nitride, Science **372**, 1458 (2021).

[32] J. Liu, Y. Zhou, S. Yepez Rodriguez, M. A. Delmont, R. A. Welser, T. Ho, N. Sirica, K. McClure, P. Vilmercati, J. W. Ziller, *et al.*, Controllable strain-driven topological phase transition and dominant surface-state transport in $HfTe_5$, Nat. Commun. **15**, 332 (2024).

[33] K. Jia, X.-J. Dong, S.-S. Li, W.-X. Ji, and C.-W. Zhang, Strain-engineering induced topological phase transitions and multiple valley states in Janus monolayer $VCSiN_4$, J. Mater. Chem. C **11**, 10359 (2023).

[34] Z. He, R. Peng, Y. Dai, B. Huang, and Y. Ma, Single-layer ScI_2: A paradigm for valley-related multiple Hall effect, Appl. Phys. Lett. **119**, 243102 (2021).

[35] Y. Tian, C.-B. Wang, B.-Y. Zhang, X. Kong, and W.-J. Gong, Quantum layer spin Hall effect in sliding antiferromagnetic bilayers, J. Mater. Chem. C **12**, 10950 (2024).

[36] J. Bai, T. Yang, Z. Guo, Y. Liu, Y. Jiao, W. Meng, and Z. Cheng, Controllable topological phase transition *via* ferroelectric–paraelectric switching in a ferromagnetic single-layer $M_IM_{II}Ge_2X_6$ family, Mater. Horiz. **12**, 2248 (2025).

[37] R. Li, N. Mao, L. Cai, Y. Bai, B. Huang, Y. Dai, and C. Niu, Ferroelectric heterobilayer with tunable first- and higher-order topological states, Phys. Rev. B **108**, 125302 (2023).

[38] X. Duan, Z. Zhu, X. Chen, Z. Song, and J. Qi, Nonvolatile electric-field control of topological phase transition in a two-dimensional ferroelectric heterostructure, J. Mater. Chem. C **12**, 6278 (2024).

[39] G. Kresse and J. Furthmüller, Efficient iterative schemes for *ab initio* total-energy calculations using a plane-wave basis set, Phys. Rev. B **54**, 11169 (1996).

[40] G. Kresse and J. Furthmüller, Efficiency of ab-initio total energy calculations for metals and semiconductors using a plane-wave basis set, Comput. Mater. Sci. **6**, 15 (1996).

[41] J. P. Perdew, K. Burke, and M. Ernzerhof, Generalized gradient approximation made simple, Phys. Rev. Lett. **77**, 3865 (1996).

[42] S. L. Dudarev, G. A. Botton, S. Y. Savrasov, C. J. Humphreys, and A. P. Sutton, Electron-energy-loss spectra and the structural

stability of nickel oxide: An LSDA+U study, Phys. Rev. B **57**, 1505 (1998).

[43] M. Cococcioni and S. de Gironcoli, Linear response approach to the calculation of the effective interaction parameters in the LDA + U method, Phys. Rev. B **71**, 035105 (2005).

[44] S. Grimme, J. Antony, S. Ehrlich, and H. Krieg, A consistent and accurate *ab initio* parametrization of density functional dispersion correction (DFT-D) for the 94 elements H-Pu, J. Chem. Phys. **132**, 154104 (2010).

[45] A. A. Mostofi, J. R. Yates, Y.-S. Lee, I. Souza, D. Vanderbilt, and N. Marzari, Wannier90: A tool for obtaining maximally-localised Wannier functions, Comput. Phys. Commun. **178**, 685 (2008).

[46] Q. Wu, S. Zhang, H.-F. Song, M. Troyer, and A. A. Soluyanov, WannierTools: An open-source software package for novel topological materials, Comput. Phys. Commun. **224**, 405 (2018).

[47] See Supplemental Material at http://link.aps.org/supplemental/10.1103/hrmc-wzkq for (I) tight-binding model, (II) computational details, (III) MX_2 materials energy band comparison, (IV) higher-order topological corner charge, (V) layer-projected operator and layer-projected topological invariants, which includes Refs. [18,43,48,49].

[48] E. Prodan, Robustness of the spin-Chern number, Phys. Rev. B **80**, 125327 (2009).

[49] J. E. Avron, R. Seiler, and B. Simon, Homotopy and quantization in condensed matter physics, Phys. Rev. Lett. **51**, 51 (1983).

[50] R. Li, N. Mao, X. Wu, B. Huang, Y. Dai, and C. Niu, Robust second-order topological insulators with giant valley polarization in two-dimensional honeycomb ferromagnets, Nano Lett. **23**, 91 (2023).

[51] Y. Wu, J. Tong, L. Deng, F. Luo, F. Tian, G. Qin, and X. Zhang, Coexisting ferroelectric and ferrovalley polarizations in bilayer stacked magnetic semiconductors, Nano Lett. **23**, 6226 (2023).

[52] X.-J. Dong and C.-W. Zhang, Interlayer coupling of valley and layer in the homostructure bilayer ScI_2, Phys. Chem. Chem. Phys. **27**, 13686 (2025).

[53] X. Chen, J. Ren, Y. Zhu, Y. Yu, A. Zhang, P. Liu, J. Li, Y. Liu, C. Li, and Q. Liu, Enumeration and representation theory of spin space groups, Phys. Rev. X **14**, 031038 (2024).

[54] G.-B. Liu, W.-Y. Shan, Y. Yao, W. Yao, and D. Xiao, Three-band tight-binding model for monolayers of group-VIB transition metal dichalcogenides, Phys. Rev. B **88**, 085433 (2013).

[55] J. Ji, G. Yu, C. Xu, and H. J. Xiang, General theory for bilayer stacking ferroelectricity, Phys. Rev. Lett. **130**, 146801 (2023).

[56] D. Xiao, G.-B. Liu, W. Feng, X. Xu, and W. Yao, Coupled spin and valley physics in monolayers of MoS_2 and other group-VI dichalcogenides, Phys. Rev. Lett. **108**, 196802 (2012).

[57] K. Liu, X. Ma, Y. Li, and M. Zhao, Tailoring the quantum anomalous layer Hall effect in multiferroic bilayers through sliding, npj Comput. Mater. **10**, 118 (2024).

[58] D. Xiao, M.-C. Chang, and Q. Niu, Berry phase effects on electronic properties, Rev. Mod. Phys. **82**, 1959 (2010).

[59] M. Costa, B. Focassio, L. M. Canonico, T. P. Cysne, G. R. Schleder, R. B. Muniz, A. Fazzio, and T. G. Rappoport, Connecting higher-order topology with the orbital Hall effect in monolayers of transition metal dichalcogenides, Phys. Rev. Lett. **130**, 116204 (2023).

[60] D. J. Thouless, M. Kohmoto, M. P. Nightingale, and M. den Nijs, Quantized Hall conductance in a two-dimensional periodic potential, Phys. Rev. Lett. **49**, 405 (1982).

[61] Y. Yao, L. Kleinman, A. H. MacDonald, J. Sinova, T. Jungwirth, D.-s. Wang, E. Wang, and Q. Niu, First principles calculation of anomalous Hall conductivity in ferromagnetic BCC Fe, Phys. Rev. Lett. **92**, 037204 (2004).

[62] J. R. Yates, X. Wang, D. Vanderbilt, and I. Souza, Spectral and Fermi surface properties from Wannier interpolation, Phys. Rev. B **75**, 195121 (2007).

[63] N. Miao, B. Xu, L. Zhu, J. Zhou, and Z. Sun, 2D intrinsic ferromagnets from van der Waals antiferromagnets, J. Am. Chem. Soc. **140**, 2417 (2018).

[64] C. Gong, P. Zhang, T. Norden, Q. Li, Z. Guo, A. Chaturvedi, A. Najafi, S. Lan, X. Liu, Y. Wang, *et al.*, Ferromagnetism emerged from non-ferromagnetic atomic crystals, Nat. Commun. **14**, 3839 (2023).